

# Topology Aware Neural Interpolation of Scalar Fields

Mohamed Kissi\*, Keanu Sisouk†, Joshua A. Levine‡ and Julien Tierny§

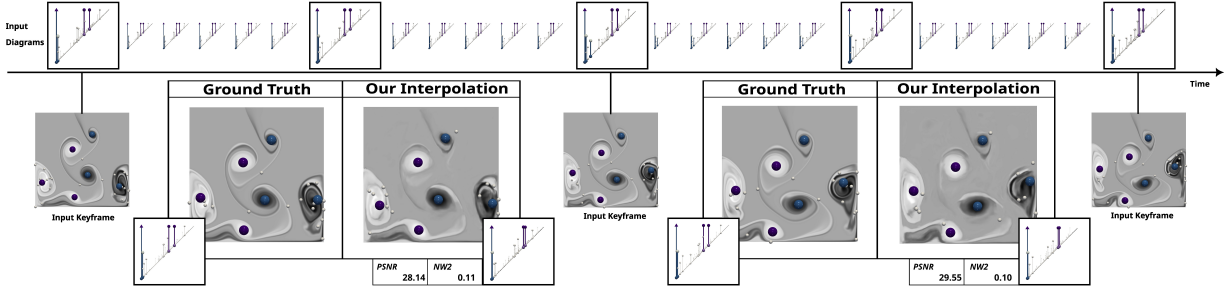


Figure 1: Given a time-varying sequence of persistence diagrams (top), along with a sparse set of corresponding *keyframe* scalar fields (“Input Keyframe” labels), our interpolation approach aims at “inverting” the *non-keyframe* diagrams and generating plausible estimations of the missing, *non-keyframe* scalar fields (“Our Interpolation” labels) enabling their visualization and analysis.

## ABSTRACT

This paper presents a neural scheme for the topology-aware interpolation of time-varying scalar fields. Given a time-varying sequence of persistence diagrams, along with a sparse temporal sampling of the corresponding scalar fields, denoted as *keyframes*, our interpolation approach aims at “inverting” the *non-keyframe* diagrams to produce plausible estimations of the corresponding, missing data. For this, we rely on a neural architecture which learns the relation from a time value to the corresponding scalar field, based on the keyframe examples, and reliably extends this relation to the *non-keyframe* time steps. We show how augmenting this architecture with specific topological losses exploiting the input diagrams both improves the geometrical and topological reconstruction of the *non-keyframe* time steps. At query time, given an input time value for which an interpolation is desired, our approach instantaneously produces an output, via a single propagation of the time input through the network. Experiments interpolating 2D and 3D time-varying datasets show our approach superiority, both in terms of data and topological fitting, with regard to reference interpolation schemes.

**Index Terms:** Temporal interpolation, neural networks, topological data analysis, persistence optimization.

## 1 INTRODUCTION

As computational resources and acquisition devices are more efficient and precise, datasets are growing in resolution and details. This results in a growth in the size of datasets which challenges their storage, processing and analysis. To address this issue, *data reduction* is commonly considered, either by employing lossy compression schemes [48, 3] or by storing reduced data representations, which concisely, yet precisely, only encode the core features of the data, possibly during data production (i.e., *in-situ* [6, 2]).

Topological Data Analysis (TDA) [17] precisely focuses on the robust encoding of the structural patterns of a dataset into concise *topological descriptors*, whose successful applications have been

documented in a variety of domains and contexts [36]. Topological descriptors are often used as a mean of data reduction, typically by storing to disk these descriptors instead of the data itself. For instance, for time-varying datasets, a typical strategy [8, 9, 20] consists in storing the actual data at a low frequency (resulting in the storage of a small number  $n$  of *keyframes*), while storing topological descriptors at a higher frequency (e.g., for a large number  $N \gg n$  of *non-keyframe* time steps). Then, the produced descriptors can be directly post-processed by dedicated statistical frameworks [80, 45, 87, 65, 66, 64], tailored to the analysis of topological representations. However, in many scenarios, a complete investigation might require going back to the original dataset which initially generated a given topological descriptor, for instance, for further visual inspection, interpretation and analysis. Then, the following question arises: *how can we reliably “invert” the construction of a topological descriptor?* (i.e., retrieve the dataset which generated it). Unfortunately, this inverse problem is ill-posed as many distinct datasets can generate the same topological descriptor (see Fig. 3). Then, further constraints need to be considered to exploit the available data, e.g., the stored *keyframes*.

This work addresses this issue by presenting a topology-aware interpolation approach. Given a reduced representation of an input time-varying scalar field (i.e., the persistence diagram of each time-step and a few *keyframes*), the overall goal of our work is to *invert* the *non-keyframe* diagrams. To achieve this goal, we exploit a generative neural architecture to interpolate the scalar field for a given time step. This network is trained to learn the relation from the time parameter to the input time varying scalar field, based on the keyframe examples, in order to reliably extend this relation to the *non-keyframes*. Also, we show how augmenting this architecture with specific topology-aware losses exploiting the input diagrams both improves the geometrical and topological reconstruction of the *non-keyframe* time steps. At query time, our approach only requires as an input the time value for which an interpolation is desired and it instantaneously produces an interpolated scalar field, via a single propagation of the time through the neural network. Experiments interpolating 2D and 3D time-varying ground-truth datasets demonstrate the superiority of our model, both in terms of data and topological fitting, with regard to previous, baseline and neural interpolation schemes providing comparable query times.

### 1.1 Related work

This section reviews the literature related to our work, which can be classified into the following main categories.

\*CNRS, Sorbonne Université - mohamed.kissi@sorbonne-universite.fr

†CNRS, Sorbonne Université - keanu.sisouk@sorbonne-universite.fr

‡University of Arizona - josh@cs.arizona.edu

§CNRS, Sorbonne Université - julien.tierny@sorbonne-universite.fr

**Topological methods in visualization:** The visualization community has been investigating Topological Data Analysis (TDA) [17] for more than two decades [36], with applications to a variety of domains, including combustion [8] fluid dynamics [55] material sciences [72], chemistry [59], or astrophysics [71] to name a few. A key feature of TDA is its ability to robustly extract the structural patterns present in complex datasets and to efficiently represent them into concise representations. Such representations include persistence diagrams [29], merge [53] and contour trees [27], Reeb graphs [28], or Morse-Smale complexes [70]. Moreover, another critical aspect of TDA is its ability to provide multi-scale hierarchies of the above topological data representations, enabling in consequence a multi-scale visualization, exploration and analysis of the topological features of the data. In that context, *topological persistence* [18] is an established importance measure which can be directly read from the persistence diagram and which can be used to drive the simplification of the above topological representations.

In many application scenarios, when handling time-varying data in scientific computing [8, 9, 20] (in particular *in-situ* [6, 2]), these topological descriptors are often used as *proxies* to the data for the purpose of data reduction. For instance, in the context of simulating mosquito-borne disease spread, Brown et al. [9] store time steps of the data at a low frequency to reduce IO, while the persistence diagram (which is orders of magnitude smaller than the original data) is stored permanently at a higher frequency. Similar data reduction strategies based on the merge tree have also been documented [8]. Then, in a post-process, the resulting ensemble of topological proxies can be exploited by statistical frameworks [80, 45, 87, 65, 66, 64] which are tailored to the analysis of topological descriptors. In this work, we focus on exploiting these topological data representations (in particular persistence diagrams), in conjunction with a sparse temporal sampling of the actual data, to generate plausible visualizations of the missing, unstored data, in a way that favors topological feature preservation. For this, we rely on a neural scheme which integrates topological constraints, thanks to persistence optimization [67, 22, 10, 74, 56, 44], as described in Sec. 3. Note that several schemes have been investigated for achieving topology-aware compression [73, 47]. However, to our knowledge no compression algorithm has been documented for the preservation of saddle-saddle pairs (a specific type of features handled in our work). Also, compression is a problem that is *orthogonal* to the setup studied in our work. First, compressors have access to the *full* input data, which eases several aspects dealing with topology enforcement and data value preservation. In contrast, our approach does *not* have access to the full input data but only to a reduced representation (the persistence diagram of each time step, as well as a few *keyframes*). Second, compression could be used in *conjunction* to our work, e.g., by using topology-aware compressors to store the *keyframes*.

**Neural methods for interpolation:** The problem of interpolating fields in time appears frequently in both vision and visualization.

In computer vision, the idea of interpolating video frames from a sequence of images is a well known research topic, showing up applications such as producing slow-motion videos, temporal upsampling, and video compression. A recent survey [15] categorizes approaches into two high level categories: flow-based methods (which rely on an estimation of optical flow [52]) and kernel-based methods (which rely on evaluating differences in a fixed neighborhood of each pixel). This dichotomy is conceptually similar to Lagrangian vs. Eulerian methods, as observed by Meyer et al. [54] who also propose looking at phase-based methods for video interpolation.

When working in the setting of video, there are sharper differences than one might consider for field data. Typically, video footage is assumed to be objects moving around in a scene, and thus it is reasonable to use an optical-flow based model that tracks the trajectories and velocities of individual pixels (as ob-

ject samples). Techniques to compute optical flow have seen significant advances when using deep learning methods such as FlowNet [16, 38], PWC-Net [75], and RAFT [77]. While these form an impressive backbone to many video interpolation techniques [40, 4, 49, 57, 60, 61, 37, 68], they also can come at the cost of complex optimization procedures. Because of the framing of bidirectional flow, often these methods are limited to synthesizing single (or a fixed number of) frames between two input frames, and they also make relatively strong assumptions (reasonable for videos of objects) that pixel movement should be captured with flow.

Kernel-based methods [46, 58, 13, 42], focus instead on localized difference in pixel values within a neighborhood, but as a result often cannot estimate motion accurately if between-frame movement is larger than the kernel size. The method VideoINR considers interpolating videos in both space and time simultaneously [12]. Closely related to our approach is the idea of modeling a video as a function in time, as proposed by Chen et al. in NeRV [11]. We also consider the idea of modeling a time-varying field as a network conditioned to produce an entire frame given a time step; however, for our work we model the “frame” as a 3D volume, and we guide the optimization of the network with a topological loss. Notably, recent work in visualization has also built upon NeRV, such as NeRVi [26] and FCNR [50], but these works focus on building neural models for rendered images (2D) of time-varying volumes, rather than modeling the volume itself.

While most applications in computer vision are limited to 2D + time, some of these methods have been extended to 3D + time images, particularly coming from medical imaging [30, 85]. Yin et al. considered adapting some of the above methods directly to the setting of coronary angiography [88]. More generally, to address modeling volumetric data, in visualization numerous authors have begun to consider machine learning methods for time-varying volumes. TSR-TVD is recent work in this space utilizing recurrent generative models for temporal super resolution [31]. Han et al. later considered the generalized problem of spatio-temporal super-resolution in STNet [34]. Both methods suffer from long training times and only produce a fixed temporal scale factor, suffering from the same limitations as many video interpolation methods. STSR-Net employs a two-stage framework using optical flow for spatial-temporal super resolution [1]. Recently, FLINT [23] also used optical flow for temporal super resolution, building upon RIFE [37].

Following the introduction of implicit neural representation (INRs) to the visualization community for volume compression by Lu et al. [51], numerous authors considered their use in other applications. CoordNet leveraged INRs for multiple visualization tasks (including spatio-temporal super resolution and visualization synthesis) for time-varying ensembles [32]. While this approach produced a generalized framework, to address large training times and model sizes, different authors considered using knowledge distillation for either learning hypernetworks [86] or compressed models [33] with CoordNet serving as the teacher model. FFEINR [41] considered an INR for joint spatio-temporal super resolution based on VideoINR [12]. Finally, STSR-INR is a recent neural method for spatio-temporal super resolution, supporting multivariate ensemble data [76]. We consider STSR-INR as a representative example of state-of-the-art INRs to compare against, although it differs from our work in that it does not explicitly consider a loss based on topological features. Including such a loss directly into a coordinate-based network (that predicts positional samples of the field in batches, rather than an entire volume) would require a significantly more costly loss function.

## 1.2 Contributions

This paper makes the following new contributions:

1. An approach combining (i) a generative neural model for scalar field interpolation with (ii) topological losses based on

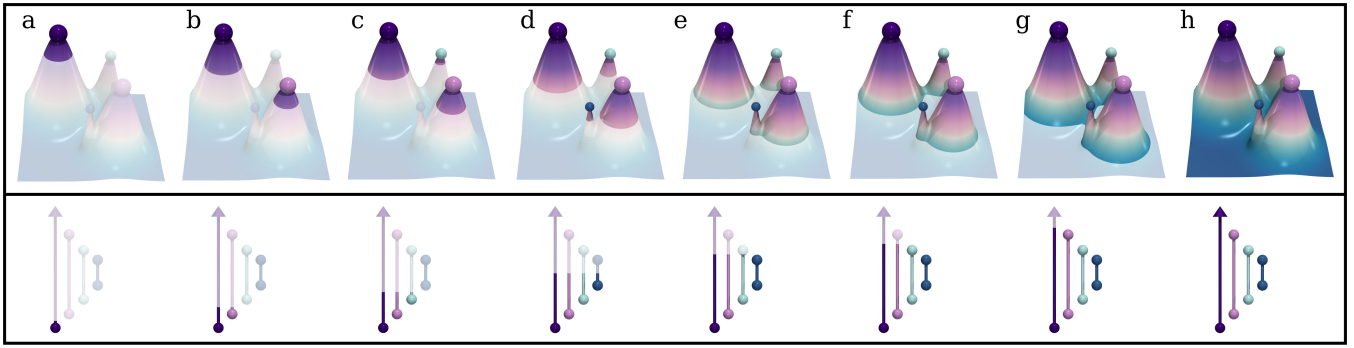


Figure 2: Filtration of the opposite elevation function (going downward, purple: low values, cyan: high values) on a toy terrain example (in transparent). From left to right, simplices are progressively added in the filtered simplicial complex for increasing values of opposite elevation. Each local minimum triggers the *birth* of a connected component in the complex (sub-figures a to d). Connected components are represented by growing bars of matching color in the diagram (bottom). When a component merges with an *older* one (sub-figures e, f and g), its corresponding bar terminates its growth in the diagram and the corresponding topological feature is said to *die* at the corresponding value.

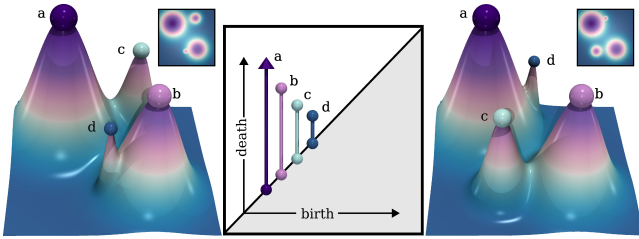


Figure 3: Scalar fields (height opposite) admitting a common persistence diagram (center). Each hill is encoded in the diagram by a vertical bar whose length encodes the *persistence* of the corresponding topological feature in the data (arrows indicate generators with infinite persistence). While the diagram encodes the list of topological features with their birth, death and persistence, it forgets their geometrical realization in the data.

persistence diagrams, for constraining the topology *and* geometry of the output interpolations.

2. A TTK/PyTorch implementation for reproducibility.

## 2 BACKGROUND

This section provides the required technical background in Topological Data Analysis (TDA). For further readings, we refer the reader to textbooks on computational topology [17].

### 2.1 Input data

Each input dataset is typically provided as a scalar field  $f : \mathcal{C} \rightarrow \mathbb{R}$ , valued on the vertices of a cubical complex  $\mathcal{C}$  (i.e., a 2D or 3D regular grid). In practice, for implementation genericity purposes,  $\mathcal{C}$  is often triangulated (via an on-the-fly emulation [78]) into a simplicial complex  $\mathcal{K}$  (typically, with the Freudenthal triangulation). This yields a piecewise linear (PL) scalar field  $\rho : \mathcal{K} \rightarrow \mathbb{R}$ , valued on the vertices of  $\mathcal{K}$  and linearly interpolated on the simplices of higher dimensions. In practice, the data values are given as a *data vector*, noted  $v_f \in \mathbb{R}^{n_v}$  (where  $n_v$  is the number of vertices in  $\mathcal{K}$ ). Additionally,  $f$  is required to be injective on the vertices, which is achieved via a variant of simulation of simplicity [19]. Also, in our experiments,  $f$  will be normalized (i.e., valued between 0 and 1) to ease parameter tuning across datasets.

### 2.2 Persistence diagrams

Persistent homology emerged independently from multiple research groups [5, 21, 69, 18]. Conceptually, it analyzes a pro-

gressive sweep of the data (called *filtration*), and computes at each stage its associated topological features (specifically, its *homology generators*). Additionally, it establishes correspondences between features detected at successive steps. This allows for the identification of topological features along with their duration throughout the filtration process.

In our work, we rely on the lexicographic filtration of the input scalar data, which sorts simplices by extending the global order on the vertices (based on their  $f$  values) to the simplices (see [29]). This induces a nested sequence of simplicial complexes  $\emptyset = \mathcal{K}_0 \subset \mathcal{K}_1 \subset \dots \subset \mathcal{K}_{n_\sigma} = \mathcal{K}$  (with  $n_\sigma$  being the number of simplices in  $\mathcal{K}$ ).

At each stage  $i$  of the filtration, for a given  $p^{\text{th}}$  homology group, one can track the corresponding *homology generators*, whose number defines the  $p^{\text{th}}$  Betti number  $\beta_p$ . In low dimensions (e.g., 3D), this quantity is accompanied with a simple intuition:  $\beta_0$  encodes the number of connected components,  $\beta_1$  that of topological handles and  $\beta_2$  that of cavities in  $\mathcal{K}_i$ . Given two consecutive steps  $i$  and  $j$  of the filtration, since the corresponding simplicial complexes  $\mathcal{K}_i$  and  $\mathcal{K}_j$  are nested, one can easily establish a correspondence (i.e., a *homomorphism*) between the generators observed at step  $i$  and those observed at step  $j$ . In particular, a *persistent generator* is said to be born at step  $j$  if it has not been matched to any generator pre-existing at step  $i$ . By symmetry, a generator is said to die at step  $j$  if it merges with another older homology class (born before it). Then, each  $p$ -dimensional persistent generator is accompanied by a pair of simplices  $(\sigma_b, \sigma_d)$  called *persistence pair*, which corresponds to the  $p$  and  $(p+1)$  simplices inserted in the filtration at the birth and death of the generator. The *persistence* of the pair is given by  $p(\sigma_b, \sigma_d) = v_f[v_d] - v_f[v_b]$ , where  $v_b$  and  $v_d$  are the *birth* and *death* vertices of the pair (i.e., the highest vertices in  $\sigma_b$  and  $\sigma_d$ ). Note that the generators characterizing the homology groups of the input complex  $\mathcal{K}$  are said to have *infinite persistence*. This process is illustrated in Fig. 2 for the specific case of the 0-dimensional persistent homology (representing persistent connected components).

The *persistence diagram* is a concise encoding of the persistence pairs of a scalar field (Fig. 2). It represents each pair by a vertical bar, whose bottom point is placed on the diagonal and whose top point is placed at coordinate  $(v_f[v_b], v_f[v_d])$ . Bars representing generators with infinite persistence are cropped at the maximum  $f$  value. Note that, as discussed in the introduction, the pre-image of the construction of a persistence diagram is not unique. This is shown in Fig. 3, where two distinct scalar fields produce the same diagram. This further illustrates the ill-posedness of inverting the construction of persistence diagrams.

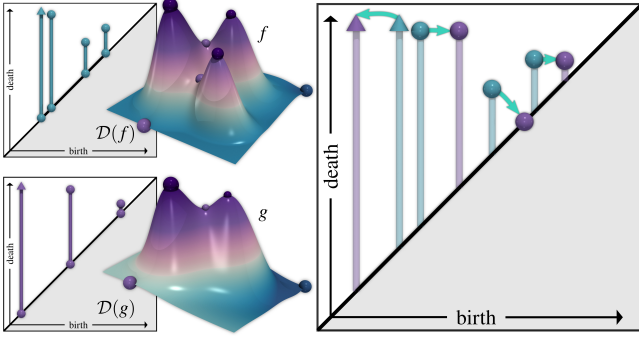


Figure 4: The Wasserstein distance  $\mathcal{W}_2$  between  $\mathcal{D}(f)$  (top) and  $\mathcal{D}(g)$  (bottom) is obtained by assignment optimization (Eq. 1) in the birth-death plane (right). The optimal assignment  $\phi^*$  (arrows) defines a least-effort deformation of  $\mathcal{D}(f)$  into  $\mathcal{D}(g)$ , by moving persistence pairs in the plane.

### 2.3 Wasserstein distance between diagrams

The *Wasserstein distance* (Fig. 4) is an established metric for comparing two diagrams  $\mathcal{D}(f)$  and  $\mathcal{D}(g)$  [17]. To facilitate its computation, the input diagrams first need to be *augmented*, to guarantee that they count the same number of points. This process is achieved as follows. Given a point  $p = (p_b, p_d) \in \mathcal{D}(f)$ , let  $\Delta(p)$  be its diagonal projection:  $\Delta(p) = (\frac{1}{2}(p_b + p_d), \frac{1}{2}(p_b + p_d))$ . We note  $\Delta_f$  and  $\Delta_g$  the sets of the diagonal projections of the points of  $\mathcal{D}(f)$  and  $\mathcal{D}(g)$ . Then,  $\mathcal{D}(f)$  and  $\mathcal{D}(g)$  are *augmented* by adding to each of them the set of diagonal points  $\Delta_g$  and  $\Delta_f$  respectively. After this step, we have  $|\mathcal{D}(f)| = |\mathcal{D}(g)|$ .

Then, given two augmented persistence diagrams  $\mathcal{D}(f)$  and  $\mathcal{D}(g)$ , the  $L^q$  Wasserstein distance between them is defined as:

$$\mathcal{W}_q(\mathcal{D}(f), \mathcal{D}(g)) = \min_{\phi \in \Phi} \left( \sum_{p \in \mathcal{D}(f)} c(p, \phi(p))^q \right)^{\frac{1}{q}}, \quad (1)$$

where  $\Phi$  is the set of bijections from  $\mathcal{D}(f)$  to  $\mathcal{D}(g)$ , such that points of finite (respectively infinite)  $r$ -dimensional persistent generators are mapped to points of finite (respectively infinite)  $r$ -dimensional persistent generators. In particular, the cost  $c(p, p')$  is set to 0 when both  $p$  and  $p'$  are diagonal points (i.e., dummy features). Otherwise, it is set to the Euclidean distance in the birth-death plane  $\|p - p'\|_2$ .

To analyze our experimental results (Sec. 4), in particular to compare topology preservation across multiple datasets, we will consider the following normalization:

$$\mathcal{N}\mathcal{W}_q(\mathcal{D}(f), \mathcal{D}(g)) = \frac{\mathcal{W}_q(\mathcal{D}(f), \mathcal{D}(g))}{\left( \mathcal{W}_q(\mathcal{D}(f), \mathcal{D}_\emptyset)^q + \mathcal{W}_q(\mathcal{D}_\emptyset, \mathcal{D}(g))^q \right)^{\frac{1}{q}}},$$

where  $\mathcal{D}_\emptyset$  is the empty diagram. This quantity is 0 when  $\mathcal{D}(f)$  and  $\mathcal{D}(g)$  are identical and 1 when there is no matching between the features of the diagrams (i.e., when the optimal assignment only sends points to/from the diagonal).

### 2.4 Persistence optimization

Persistence optimization has been investigated by several authors [67, 22, 10, 74, 56]. We recap here an efficient and generic framework [10], which has been recently exploited in visualization [44] and which is used by our work to enforce topological constraints.

The goal of persistence optimization is to modify an input data vector  $v_f \in \mathbb{R}^{n_v}$  (Sec. 2.1), such that its persistence diagram  $\mathcal{D}(f)$  minimizes the considered loss  $\mathcal{L}$ . For that,  $\mathcal{L}$  is typically decomposed into several steps. First, we call the *filtration map* the function  $\mathcal{F} : \mathbb{R}^{n_v} \rightarrow \mathbb{R}^{n_\sigma}$ , which maps a data vector  $v_f$  to a filtration,

encoded as a vector  $\mathcal{F}(v_f) \in \mathbb{R}^{n_\sigma}$ , which stores in its  $i^{\text{th}}$  entry the global lexicographic order (Sec. 2.2) of the  $i^{\text{th}}$  simplex of  $\mathcal{K}$ . In practice, a *backward filtration map*, noted  $\mathcal{F}^+ : \mathbb{R}^{n_\sigma} \rightarrow \mathbb{R}^{n_v}$ , is also maintained. It maps a filtration vector  $\mathcal{F}(v_f)$  back to a vector in  $\mathbb{R}^{n_v}$ , whose  $i^{\text{th}}$  entry is the index of the highest vertex (in global vertex order) of the  $i^{\text{th}}$  simplex in the global lexicographic order. Next, a *persistence map*  $\mathcal{P} : \mathbb{R}^{n_\sigma} \rightarrow \mathbb{R}^{n_\sigma}$  maps a filtration vector  $\mathcal{F}(v_f)$  to a vector  $\mathcal{P}(\mathcal{F}(v_f))$ . In particular, the  $i^{\text{th}}$  entry of this map assigns the  $i^{\text{th}}$  simplex in the global lexicographic order to its *critical simplex persistence order*. That latter order is obtained as follows. First, the points of  $\mathcal{D}(f)$  are sorted by *diagram order*, i.e., by increasing birth and then by increasing death (to disambiguate ties). The persistence pairs are then sorted with this order, by interleaving the birth and death simplices of each diagram point. This provides an ordering of the critical simplices, called the *critical simplex persistence order*, where the  $(2i)^{\text{th}}$  and  $(2i+1)^{\text{th}}$  entries encode respectively the birth and death simplices of the  $i^{\text{th}}$  point  $p_i$  in the diagram order. Critical simplices corresponding to homology classes of infinite persistence are added at the end of this list, in increasing order of  $f$  values. Finally, in the persistence map, the entries corresponding to regular simplices are set to  $-1$ .

Now, let us consider a generic energy term  $\mathcal{E} : \mathbb{R}^{n_\sigma} \rightarrow \mathbb{R}$ , which given a persistence map (defined above), evaluates the relevance of the corresponding diagram  $\mathcal{D}(f)$  for the considered problem. Then, given an input vector  $v_f$ , the associated loss  $\mathcal{L} : \mathbb{R}^{n_v} \rightarrow \mathbb{R}$  is:

$$\mathcal{L}(v_f) = \mathcal{E} \circ \mathcal{P} \circ \mathcal{F}(v_f).$$

As discussed in [10], if  $\mathcal{E}$  is locally Lipschitz and a definable function of persistence, then we have the guarantee that the composition  $\mathcal{E} \circ \mathcal{P} \circ \mathcal{F}$  is also definable and locally Lipschitz [10], which itself guarantees that the generic loss  $\mathcal{L}$  is differentiable almost everywhere. Then, stochastic gradient descent [43] can be employed with guaranteed convergence [14]. Assuming a constant global lexicographic order, the loss is minimized by displacing each point  $p_i$  in the diagram  $\mathcal{D}(f)$  according to the gradient. Concretely, this displacement is back-propagated in the data vector  $v_f$ , by identifying the vertices  $v_{i_b}$  and  $v_{i_d}$  corresponding to the birth and death of the  $i^{\text{th}}$  point in the diagram order:

$$\begin{aligned} v_{i_b} &= \mathcal{F}^+(\mathcal{P}^{-1}(2i)) \\ v_{i_d} &= \mathcal{F}^+(\mathcal{P}^{-1}(2i+1)), \end{aligned}$$

and by updating their data values  $v_f(v_{i_b})$  and  $v_f(v_{i_d})$  according to the gradient. This back-propagation mechanism (updating the input vector  $v_f$  to decrease the loss  $\mathcal{L}$ ) ensures that persistence optimization can be used in conjunction with the automatic differentiation features of neural networks [62], thereby enabling their training via gradient descent [43], possibly in conjunction to extra regularization terms, as described next.

## 3 APPROACH

This section presents our overall interpolation technique, given an input time-varying sequence of persistence diagrams, along with a sparse temporal sampling of the corresponding scalar fields. While the neural network architecture exploited in our approach is typical of related work [11], we still document its specifications in Sec. 3.2 for completeness and reproducibility purposes.

### 3.1 Overview

Our approach relies on a generative neural network architecture, referred to in the remainder as *TimeToScalarField*. It is presented in Sec. 3.2 and schematically illustrated in Fig. 5. It takes as an input a time parameter value  $t \in [0, 1]$ , and generates a scalar data vector  $v_{f(t)} \in \mathbb{R}^{n_v}$  defining a scalar field  $f(t)$  on a cubical complex  $\mathcal{C}$  (i.e.,



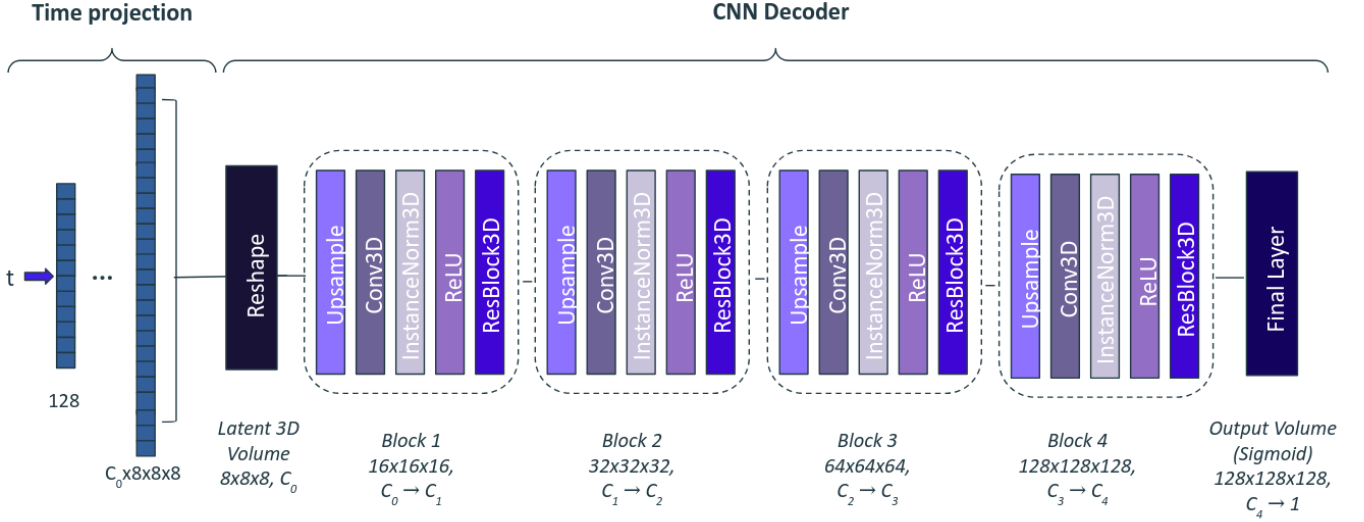


Figure 5: *TimeToScalarField*: An input value  $t$  is encoded using sinusoidal positional encoding and projected through a fully connected layer into a latent 3D tensor of size  $C_0 \times 8 \times 8 \times 8$ , where  $C_0$  denotes the initial number of channels. This tensor is processed by a CNN composed of four sequential blocks, each consisting of: (i) trilinear upsampling (by a factor of 2), (ii) 3D convolution (with kernel size  $3 \times 3 \times 3$ ), (iii) instance normalization, (iv) ReLU activation, and (v) a residual block (*ResBlock3D*, [35]). The spatial resolution is progressively increased while the number of channels is reduced. A final convolution followed by a Sigmoid activation produces the output volume (here, with resolution  $128^3$ ).

a regular grid) with dimensions  $c_x, c_y, c_z$  assumed to be multiples of powers of two (i.e.,  $n_v = c_x \times c_y \times c_z$ ).

The training of this architecture is performed on the  $N$  time-steps of the input temporal sequence, specifically with:

- the  $n \ll N$  keyframe scalar fields and persistence diagrams,
- and the  $(N - n)$  non-keyframe persistence diagrams (for which the scalar fields are *not* given).

Note that the interpolation of distinct input temporal sequences requires the training of distinct networks. The training is achieved by minimizing the overall loss presented in Sec. 3.3. In particular, this optimization is carried out by stochastic gradient descent [43], relative to the gradient of the training loss, obtained via automatic differentiation [62]. Note that for the  $(N - n)$  non-keyframes, the corresponding scalar data is not available (only the persistence diagrams are available). Therefore, the loss terms involving scalar fields (e.g., *Mean Squared Error*, MSE) are set to zero for non-keyframe time values (see Sec. 3.3). At query time, the time  $t \in [0, 1]$  for which an interpolation is desired is presented to the input of the trained neural network, which propagates it to return the vector  $v_{f(t)}$ , defining the output scalar field  $f(t) : \mathcal{C} \rightarrow \mathbb{R}$ .

### 3.2 Architecture

The *TimeToScalarField* architecture (Fig. 5) is designed to generate spatially structured scalar fields from time values. It includes (i) a time projection and (ii) a *convolutional neural network* (CNN).

**Time projection:** The input time value  $t \in [0, 1]$  is first presented to a *positional encoding* (PE) layer [24, 82] as it is often reported (and confirmed by our experiments) to improve temporal coherence. This layer is *fixed* (i.e., not optimized) and simply maps  $t$  to a high-dimensional vector  $PE(t) \in \mathbb{R}^T$ . Each entry  $i$  of this vector is a sinusoidal function of  $t$ , with increasing frequencies for increasing values of  $i$  [82]:

$$\begin{cases} [PE(t)]_{2i} = \sin(2\pi t / 10,000^{2i/T}) \\ [PE(t)]_{2i+1} = \cos(2\pi t / 10,000^{2i/T}) \end{cases}.$$

This first positional encoding  $PE(t)$  is then projected into a higher dimensional latent space  $\mathbb{R}^{C_0 \times r_0 \times r_0 \times r_0}$  (where  $r_0$  is a coarse, initial data resolution for the subsequent CNN decoder, see below) via sequential, fully connected layers with ReLU activations (“*Reshape*” layer, Fig. 5). This projection enriches the latent representation and provides a robust foundation for the subsequent decoding. Such a re-projection approach has been widely validated in conditional generative frameworks [39]. The output of that layer forms the input for the subsequent CNN decoder.

**CNN decoder:** Our CNN decoder (Fig. 5, right) reconstructs the output data progressively through successive upsampling stages. The decoder starts with a coarse resolution ( $r_0 \times r_0 \times r_0$  in 3D and  $r_0 \times r_0$  in 2D) over  $C_0$  channels (i.e.,  $C_0$  instances of the optimization, started at distinct random initializations). As recommended in the CNN literature,  $C_0$  is progressively decreased via channel-wise filtering at each stage  $i$  into  $C_i$ , until reaching 1 (see Sec. 4.1 for further discussions). The initial resolution  $r_0$  is multiplied by 2 at each stage  $i$  along each dimension until reaching the input resolution (i.e.,  $c_x \times c_y \times c_z$ ). Specifically, each processing block  $i$  (dashed boxes in Fig. 5) consists of:

1. an upsampling phase (with bilinear and trilinear interpolants in 2D and 3D respectively),
2. a convolutional block (with kernel sizes  $3 \times 3$  and  $3 \times 3 \times 3$  in 2D and 3D respectively),
3. instance normalization [81] (to reduce overfitting and improve generalization)
4. a non-linear activation (ReLU) and
5. a residual block [35] (to stabilize the training and mitigate vanishing gradient issues often encountered in deep CNNs).

### 3.3 Losses

Given a batch of input values  $t$ , the output predictions provided by the neural network are evaluated with the following overall loss:

$$\mathcal{L} = \mathcal{L}_{MSE} + \alpha \mathcal{L}_\nabla + \beta \mathcal{L}_{CV} + \gamma \mathcal{L}_{W_2}.$$

It is composed of four terms, detailed below.

**Data fitting:** This term is the traditional *Mean Squared Error* (MSE) which evaluates, only for the  $n$  keyframes (it is 0 otherwise), the fitting of each prediction  $f_{(t_k)}$  to its training keyframe  $f_k$ :

$$\mathcal{L}_{MSE} = \frac{1}{n} \sum_{k=1}^n \frac{1}{n_v} \sum_{j=1}^{n_v} \|f_{(t_k)}(v_j) - f_k(v_j)\|_2^2.$$

**Gradient fitting:** To improve the geometry of fine scale details, an additional term is considered, only for the  $n$  keyframe timesteps (it is set to 0 otherwise), to evaluate the fitting of the gradient of each network prediction  $f_{(t_k)}$  to that of its training keyframe  $f_k$ :

$$\mathcal{L}_\nabla = \frac{1}{n} \sum_{k=1}^n \frac{1}{n_v} \sum_{j=1}^{n_v} \sum_{i=1}^{n_d} \mathcal{L}_{\nabla_1} \left( (\nabla f_{(t_k)}(v_j))_i, (\nabla f_k(v_j))_i \right),$$

where  $n_d$  is the dimensionality of the dataset (in our experiments, 2 or 3), where  $\nabla$  is the vector formed by the partial derivatives of the scalar field at a vertex  $v_j$  in the geometrical domain  $\mathcal{C}$ , and where  $\mathcal{L}_{\nabla_1}$  is the so-called *smooth  $L_1$  loss* [25] (which presents the practical interest of the  $L_1$  norm, while still being differentiable in 0):

$$\mathcal{L}_{\nabla_1}(x, y) = \begin{cases} 0.5(x-y)^2, & \text{if } |x-y| < 1, \\ |x-y| - 0.5, & \text{otherwise.} \end{cases}$$

**Critical values:** For each of its bars, in addition to its birth and death values, the persistence diagram also typically encodes in practice the identifiers  $v_b$  and  $v_d$  of the vertices respectively implied in the birth and death of the corresponding topological feature (Sec. 2.2). The set of all birth and death vertices form the *critical points* of the underlying piecewise linear scalar field [17]. Specifically, the scalar value of a birth (respectively death) vertex  $v_b$  (respectively  $v_d$ ) is given by the birth (respectively death) of its bar in the diagram. This information, which is available for all the  $N$  timesteps, can be re-used to enforce the scalar value at the precise location of each critical point, helping preserve the location of the topological features in the geometrical domain (see Sec. 4.4). This can be achieved with the following loss, which evaluates, for each prediction  $f_{(t_k)}$ , the fitting between the pointwise value  $f_{(t_k)}(v_j)$  and the corresponding value  $f_k(v_j)$  given by the input persistence diagram  $\mathcal{D}_k$  for each vertex  $v_j$  in the set of critical points  $CP_k$  of  $f_k$ :

$$\mathcal{L}_{CV} = \frac{1}{N} \sum_{k=1}^N \frac{1}{n_{CP_k}} \sum_{j=1}^{n_{CP_k}} \|f_{(t_k)}(v_j) - f_k(v_j)\|_2^2.$$

**Topology correction:** To enforce topological preservation, we evaluate the topological fitting between the diagrams  $\mathcal{D}(v_{f(t_k)})$  and their target inputs  $\mathcal{D}_k$  with the Wasserstein distance (Sec. 2.3):

$$\mathcal{L}_{W_2} = \frac{1}{N} \sum_{k=1}^N \mathcal{W}_2(\mathcal{D}(f_{(t_k)}), \mathcal{D}_k).$$

This loss effectively quantifies and penalizes topological errors. Since the Wasserstein distance is a definable function of persistence [10], it can be used within the optimization framework from Sec. 2.4 (i.e.,  $\mathcal{E} = \mathcal{L}_{W_2}$ ), with guaranteed convergence [14, 10], in conjunction with the above (convex and differentiable) losses.

### 3.4 Computational details

This section provides practical details for the training of the model presented in Sec. 3.2 with regard to the overall loss described in Sec. 3.3. The training is organized into two phases:

1. *scalar field training* (with the following loss weights, Sec. 3.3:  $\alpha = 0.1$ ,  $\beta = 1$  and  $\gamma = 0$ ) and

2. *topology correction* (with loss weights:  $\alpha = 0$ ,  $\beta = 1$ ,  $\gamma = 1$ ).

This two-phase strategy is motivated by the computational effort required by the *topology correction* step (which involves the computation of a persistence diagram at each iteration). Then, this strategy first learns quickly a plausible geometry for the missing scalar fields (*scalar field training*) prior to optimizing their topology with more expensive computational efforts (*topology correction*). Also, from a practical standpoint, our initial experiments reported that this two-phase strategy improved the convergence of the training.

For each phase, the entire input ( $N$  diagrams,  $n$  keyframes) is presented to the network at each epoch, for a number  $n_1$  and  $n_2$  of epochs for the two phases respectively (see Sec. 4.1 for further discussions). The purpose of this decomposition is to first generate a good estimation of the scalar fields in phase 1, prior to refining their topology in phase 2 (which is significantly more expensive computationally). Specifically, in phase 2, the last layer of temporal projection as well as the first block of the CNN decoder are *frozen*, in order to maintain through phase 2 the large scale details learned in phase 1. Also, to mitigate overfitting and improve generalization, dropout regularization [83] is used, omitting randomly the update of a network weight, with a probability set to 0.1.

Each epoch of topology correction (phase 2) requires the computation of  $N$  persistence diagrams  $\mathcal{D}(v_{f(t_j)})$  as well as the estimation of the Wasserstein distances to their input targets  $\mathcal{D}_j$ , which is done in practice in quadratic time (with the number of vertices  $n_v$  in the output grid). To accelerate this process, we *prune* each input target diagram  $\mathcal{D}_j$  by removing its bars with a persistence (Sec. 2.2) smaller than 1% of its largest bar, which is a typical persistence thresholding in the applications. We prune similarly  $\mathcal{D}(v_{f(t_j)})$  and fix the assignment of the pruned bars to the diagonal (which is equivalent to the destruction of these noisy features). This two-stage pruning reduces the size of the diagrams and drastically accelerates the optimal assignment optimization at the basis of the Wasserstein distance computation (Sec. 2.3). Finally, we use shared-memory parallelism to compute each diagram (and its distance to its target) in a distinct task.

The minimization of the overall loss (Sec. 3.3) is performed with the Adam solver [43] (with weight decay set at  $10^{-6}$ , to mitigate overfitting), with a relatively low initial learning rate to favor a stable optimization (see Sec. 4.1 for numerical values).

Finally, this architecture (Sec. 3.2) is subject to additional meta-parameters e.g.,  $T = 128$ ,  $r_0 = 8$ . Overall, all the meta-parameters of our approach were adjusted empirically to optimize performance (see Sec. 4.1, for dataset specific parameters).

## 4 RESULTS

This section presents results obtained with a PyTorch [62] implementation of our approach, using TTK [78, 7] for persistence computation and matching. Experiments were performed in a Google Colab environment, with an Nvidia A100-SXM4 GPU (RAM: 40 GB) and an Intel Xeon CPU (2.2 GHz, 6 cores, RAM: 80 GB).

### 4.1 Test datasets

Our experiments include both synthetic and real-life time-varying 2D and 3D scalar fields. For convenience, the considered 2D (respectively 3D) datasets have all been resampled to an initial resolution of  $512^2$  (respectively  $128^3$ ). Moreover, to replicate a setting that is typical of in-situ data production [8, 9, 20], we selected as *keyframes* 10% of the time steps (i.e.,  $n = N/10$ ), uniformly distributed in the time interval  $[0, 1]$ . The remaining 90% of the time steps were considered as ground-truth data (not seen by the model during training). Specifically, we considered the following datasets.

**Gaussian mixture:** This synthetic 2D dataset counts  $N = 180$  time steps representing a mixture of six Gaussians, where the Gaussian centers (captured by persistent maxima) evolve through time. Specifically, to evaluate the robustness of our method to value

Table 1: Meta-parameters adjusted empirically to account for the variability in geometrical/temporal complexity across our datasets.

Dataset	$C_0$	$C_1$	$C_2$	$C_3$	$C_4$	$C_5$	$C_6$	Learning rate	$n_1$	$n_2$
Gaussian mixture (2D)	256	128	64	64	32	16	8	$0.5 \times 10^{-3}$	6000	100
Mixing vortices (2D)	256	128	64	64	32	16	8	$0.5 \times 10^{-3}$	6000	100
Isabel (3D)	128	64	32	32	16	—	—	$10^{-3}$	3000	100
Asteroid impact (3D)	512	256	128	64	16	—	—	$10^{-4}$	3000	100

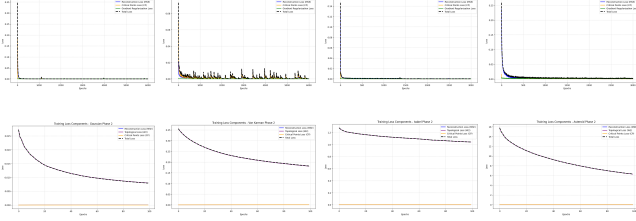


Figure 6: Loss evolution during *scalar field training* (phase 1, top) and *topology correction* (phase 2, bottom) for our datasets (from left to right: Gaussian mixture, Mixing vortices, Isabel, Asteroid impact).

changes as well as feature displacements, this dataset is decomposed into segments where only the weights of a few Gaussians evolve (i.e., making hills appear or disappear in the corresponding terrain), segments where only the center positions for a few Gaussians evolve (i.e., displacing hills in the corresponding terrain) and segments where both phenomena occur.

**Mixing vortices:** This 2D dataset counts  $N = 150$  time steps and represents the vorticity (measured as the orthogonal curl component) of a 2D flow generating a von Karman street (see [79] for downloads). This dataset has the particularity to model a 2D domain with boundaries. Then, in a first segment, the vortices of the street (captured by persistent extrema) follow a typical, common translation motion. However, in a second segment, the vortices hit the boundary and consequently start to mix together in a complicated, turbulent, whirling pattern.

**Isabel:** This 3D dataset counts  $N = 48$  time steps representing wind velocity for the Isabel hurricane [84]. To capture wind regions interacting with the boundary of the domain, we will consider as input field the opposite of the wind velocity. Then, regions associated with high winds will be captured by persistent minima of this opposite velocity. In particular, the eye of the hurricane travels through the domain into several stages (formation, drift, and landfall).

**Asteroid impact:** This 3D dataset counts  $N = 50$  timesteps and represents the impact of an asteroid with the sea at the surface of the Earth [63]. The considered scalar field is matter density, which distinguishes well the asteroid from the water and the ambient air in this simulation. In this dataset, the trajectory of the asteroid as well as the topological features resulting from the impact with the sea are captured from a topological point of view by persistent maxima.

Since these datasets exhibit distinct levels of details in terms of geometrical features and temporal variability, several meta-parameters of our approach were empirically adjusted on a per dataset basis (Tab. 1). Fig. 6 provides curves plotting the corresponding loss, for each dataset.

## 4.2 Reference approaches

We compare our technique to two approaches, selected based on their query time, which is comparable to ours (typically, below a second in practice). First, we consider as a baseline the traditional pointwise, linear interpolation with regard to time. This scheme requires the evaluation of a linear equation at each vertex of the input grid. Next, among the approaches introduced in the visualization literature, we considered STSR-INR [76], which is a recent representative of neural methods for spatio-temporal super resolution. In particular, we used the implementation provided by the authors, set

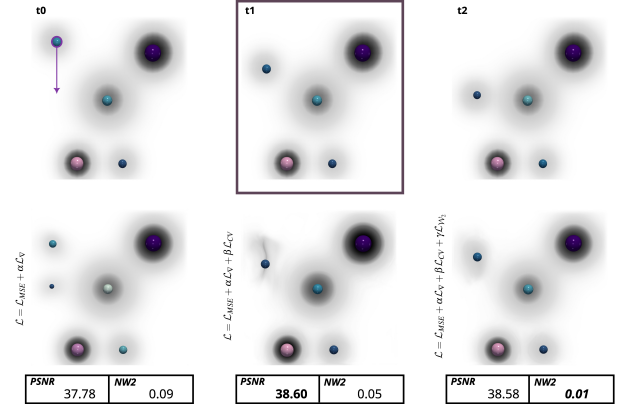


Figure 7: Influence of our individual loss terms (Sec. 3.3) on the interpolation. *Top*: Three time steps of the *Gaussian mixture* dataset (spheres: local maxima, colored and scaled by persistence). From  $t_0$  to  $t_2$ , a Gaussian center is moving down, vertically (purple arrow,  $t_0$ ). *Bottom*: Interpolations obtained for the time step  $t_1$  with different loss blending coefficients (Sec. 3.4), from left to right: (i)  $\alpha = 0.1, \beta = \gamma = 0$  (no topological loss), (ii)  $\alpha = 0.1, \beta = 1, \gamma = 0$  (critical value enforcement), (iii)  $\alpha = 0.1, \beta = 1, \gamma = 1$  (topology correction). Without our topological losses (*bottom, left*), the interpolation exhibits the *superposition artifact* typical of linear interpolation, with the moving Gaussian being replaced by two Gaussians of decreased height (at the start and end points of the displacement). Critical value enforcement (*bottom, center*) addresses this issue, resulting in one maximum in the correct location, while topology correction (*bottom, right*) improves the final geometry and topology.

up to its default recommended parameters, except for:

- the epoch number (increased to obtain similar training times);
- the model size (increased to obtain sizes also similar to ours).

The purpose of these modifications was to provide the same computational resources to both methods (STSR-INR [76] and ours). Finally, note that in both cases (linear interpolation and STSR-INR), these reference approaches have only access to the *keyframe* data.

## 4.3 Quantitative criteria

We evaluate the quantitative quality of the resulting interpolations, for the non-keyframes only, in the light of two fitting terms. First, we evaluate a *data fitting* term with the traditional *Peak Signal-to-Noise Ratio* (PSNR). Second, we evaluate a *topological fitting* term, which measures the topological accuracy of an interpolation with regard to the input target diagram, based on the normalized Wasserstein distance (Sec. 2.3). For information, we also report indicators related to the computational resources used in our experiments, namely model size (in MB) and training time (in seconds).

## 4.4 Loss influences

We start the practical analysis of our method by investigating the effects of the individual terms of our loss (presented in Sec. 3.3). Fig. 7 presents interpolation results on our synthetic dataset (*Gaussian mixture*) for various loss blending coefficients. Specifically, this figure focuses on a temporal sequence where a Gaussian center is moving down vertically (purple arrow). When using only the *MSE* and gradient losses (*bottom, left*), our method results in interpolations with a *superposition artifact* that is typical of linear interpolation: the moving Gaussian has been replaced by two Gaussians of decreased height (see the two maxima), at the start and end points of the displacement. The introduction of our loss based on the critical values reported by the input diagrams greatly

Table 2: Quantitative scores (averaged over all non-keyframe timesteps) over our test datasets for the linear interpolation, STSR-INR [76] and our method. For each score, the best value is reported in bold. Model sizes and training times are also reported.

Criterion	Method	Gaussian Mixture	Mixing vortices	Isabel	Asteroid Impact
PSNR ( $\uparrow$ )	Linear Interpolation	37.44	26.20	29.56	20.81
	STSR-INR [76]	36.18	26.17	29.05	20.06
	Our method	<b>38.58</b>	<b>29.28</b>	<b>32.41</b>	<b>22.51</b>
$\mathcal{N}W_2$ ( $\downarrow$ )	Linear Interpolation	0.12	0.40	0.62	0.56
	STSR-INR [76]	0.10	0.42	0.60	0.67
	Our method	<b>0.01</b>	<b>0.17</b>	<b>0.51</b>	<b>0.38</b>
Size (MB)	STSR-INR [76]	11	11	33	157
	Our method	11	11	33	157
Training (h.)	STSR-INR [76]	3.33	3.31	6.76	9.69
	Our method	3.20	2.76	5.70	8.96

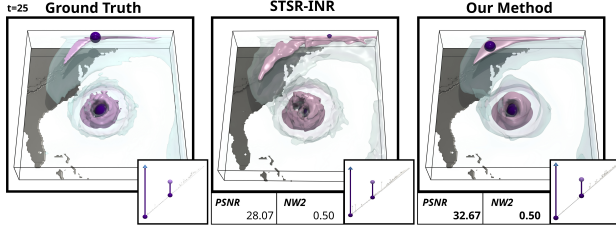


Figure 8: Comparing STSR-INR with a topological optimization post-process [44] (center) to the ground truth (left) and our method (right). To obtain a topological accuracy comparable to our method, the predictions by STSR-INR need to undergo a non-negligible optimization post-process (56 seconds) while our method is instantaneous.

contributes to addressing this issue (bottom, center). Specifically, it results in a persistent maximum, at the right value and at the right location. However, the corresponding feature exhibits a ridge-like geometry (dark curve) which does not resemble the original feature (a Gaussian, top-center). The introduction of topology correction (based on the Wasserstein distance to the input diagram, bottom right) further improves topological preservation (in terms of normalized Wasserstein distance), as well as, importantly, the geometry of the prediction: the feature associated to the moving maximum exhibits a shape that is closer visually to the original Gaussian. We assume that this geometry preservation is favored by the interplay between the topology correction (which enforces the number and persistence of features, irrespective of their location, Fig. 3) and the critical value loss (which, by enforcing critical values at specific locations, favors the appearance of topological features there).

## 4.5 Comparisons

This section provides a quantitative and qualitative comparison between our method and reference approaches (Sec. 4.2).

Tab. 2 provides an overview of the quantitative scores (averaged over all non-keyframe time steps) over our test datasets for the considered methods. This table shows that our method, by design, provides the best topological accuracy (i.e., normalized Wasserstein distance to the input diagrams). As discussed in Sec. 4.4, our topological losses (Sec. 3.3), on top of contributing to the preservation of topological features, also contribute to improving the geometry of the prediction. This is illustrated by the PSNR scores of our method, which are superior to those of the reference approaches.

Qualitative comparisons are provided in Figs. 9, 10, 11. Overall, these figures show that the linear interpolation suffers from a typical *superposition artifact*, where the two keyframes used for the interpolation are superposed on top of each other. This is particularly severe when features of interest are moving within the domain across time (which occurs in all our test datasets). This is partly addressed, sometimes successfully (Fig. 9), sometimes less successfully (Fig. 11), by the STSR-INR [76] approach, which im-

proves PSNR in some case (Fig. 9). In all cases, our approach better preserves, by design, the topological features, resulting in a superior topological accuracy. In several instances (Figs. 10, 11), our method provides the result which conforms best visually (geometrically) to the ground truth (confirming the observations of Sec. 4.4).

In principle, the results of the reference approaches (e.g., STSR-INR [76]), could be post-processed to improve their topological accuracy. This can be done, by example, by using the approach by Kissi et al. [44]. However, as shown in Fig. 8, such a post-processing step is non-negligible in terms of runtime, which significantly degrades interpolation query response times. In contrast, at query time, our approach provides a result with comparable topological accuracy instantaneously.

## 4.6 Limitations

An obvious limitation of our work, which is intrinsic to neural approaches in general (such as STSR-INR [76]), is the computational effort required for training such models, in the range of hours of computation (Tab. 2). However, for applications such as in-situ computing [6, 2], for which data storage can be a more important concern than computational effort, we believe our data reduction strategy to be still relevant, as assessed by our model sizes (Tab. 2).

Another limitation that we observed was the need for larger models for the datasets exhibiting the most geometrical and temporal complexity (Tabs. 1, 2). While it is understandable that more parameters are required in the model to capture this variability, this model size increase negatively impacts training computation times as well as model storage. Similarly, larger output sizes may require more iterations, themselves being more computationally expensive (each iteration involves a computation of persistence). Finally, our approach is currently restricted to regular grids, which is the only representation supported by our CNN-based decoding. Alternative generative architectures would need to be considered for more generic inputs, e.g., scalar fields defined on tetrahedral meshes.

## 5 CONCLUSION

This paper presented a neural approach for the topology aware interpolation of scalar fields. Our work was motivated by a data model often encountered in in-situ computing [6, 2], where snapshots of the considered time-varying data are only saved at a low frequency (every  $n$  keyframes) and where reduced representations, such as topological descriptors, are stored at a higher frequency [8, 9, 20] (every  $N \gg n$  steps). Specifically, given an input sequence of persistence diagrams and a sparse temporal sampling of the corresponding data, our approach “inverts” the non-keyframe diagrams to produce plausible estimations of the missing data. Extensive experiments showed the superiority of our method over reference approaches for preserving the topological features of interest along the interpolation. Interestingly, our experiments also revealed that our topology-aware losses could also contribute to improving the *geometry* of the interpolated data.

In the future, we will extend our experimental evaluations, by considering additional datasets and quality metrics [76]. We believe our work opens several research avenues, in particular, thanks to its instantaneous query time, for the interactive exploration of ensembles of topological descriptors, as studied in topology-tailored statistical frameworks [80, 45, 87, 65, 66, 64]. However, a multi-dimensional extension of approach (to account for more ensemble parameters than simply time) would need to be investigated.

## ACKNOWLEDGMENTS

This work is partially supported by the European Commission grant ERC-2019-COG “TORI” (ref. 863464, <https://erc-tori.github.io/>), by the U.S. Department of Energy, Office of Science, under Award Number(s) DE-SC-0023319, and by a joint graduate research fellowship (ref. 320650) funded by the CNRS and the University of Arizona.



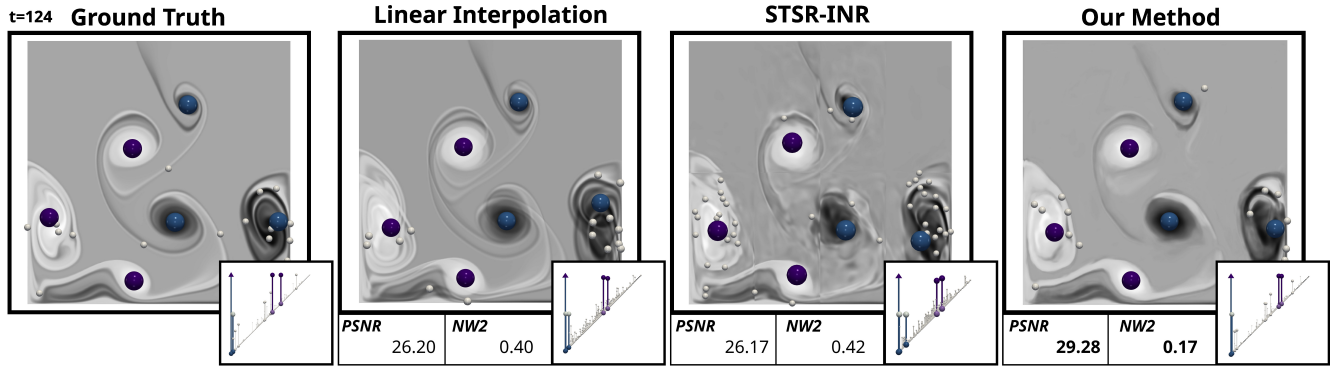


Figure 9: Comparison of temporal interpolations on the *Mixing vortices* dataset (from left to right: ground-truth, linear interpolation, STSR-INR [76] and our method). Persistent extrema are reported as colored spheres (blue: minima, purple: maxima), extrema of intermedia persistence are reported as white spheres. The persistence diagrams are reported in the bottom insets. The linear interpolation exhibits a typical *superposition artifact*, where the two keyframes used for the interpolation are superposed on top of each other. This artifact is addressed by STSR-INR, with an improved PSNR. Our method further improves PSNR, while improving topological accuracy (in particular with fewer noisy bars in the diagram).

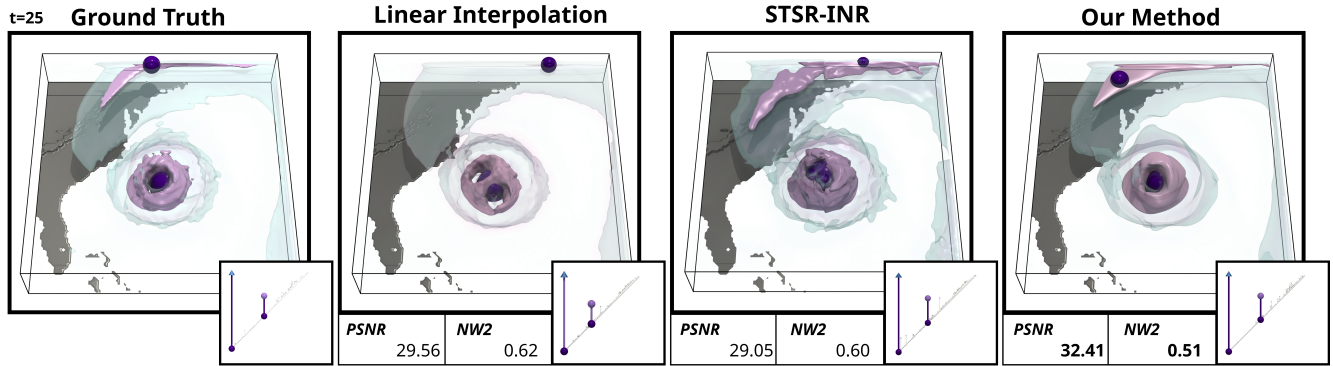


Figure 10: Comparison of temporal interpolations on the *Isabel* dataset (from left to right: ground-truth, linear interpolation, STSR-INR [76] and our method). Persistent minima of the opposite wind velocity are reported as purple spheres. A few isosurfaces are shown to represent the geometry of the data. The persistence diagrams are reported in the bottom insets. The linear interpolation exhibits its typical *superposition artifact* (similarly to Fig. 9), where the hurricane eyes from two keyframes are superposed. Moreover, it fails at capturing certain high wind regions (light purple surface, top). Here, STSR-INR produces a reconstruction with a degraded PSNR. Our method provides the best PSNR and the best topological accuracy.

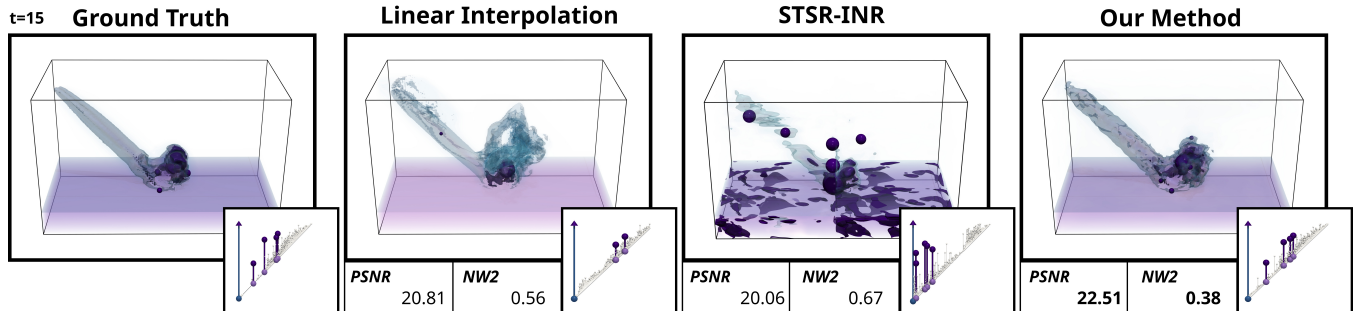


Figure 11: Comparison of temporal interpolations on the *Asteroid impact* dataset (from left to right: ground-truth, linear interpolation, STSR-INR [76] and our method). Persistent maxima are reported as purple spheres. The geometry of the data is represented via volume rendering and isosurfacing. The persistence diagrams are reported in the bottom insets. The linear interpolation exhibits its typical *superposition artifact*, where the two keyframes used for the interpolation are superposed on top of each other (similarly to Fig. 9). Here, STSR-INR produces a result with a degraded PSNR. Our method provides the indicators scores (PSNR and topological accuracy), and it provides the result which conforms best visually to the ground truth.

## REFERENCES

- [1] Y. An, H.-W. Shen, G. Shan, G. Li, and J. Liu. Stsrnet: Deep joint space-time super-resolution for vector field visualization. *IEEE CGA*, 2021. doi: 10.1109/MCG.2021.3097555
- [2] U. Ayachit, A. C. Bauer, B. Geveci, P. O’Leary, K. Moreland, N. Fabian, and J. Mauldin. ParaView Catalyst: Enabling In Situ Data Analysis and Visualization. In *ISAV*, 2015. doi: 10.1145/2828612.2828624
- [3] R. Ballester-Ripoll, P. Lindstrom, and R. Pajarola. TTHRESH: Tensor compression for multidimensional visual data. *IEEE TVCG*, 2019. doi: 10.1109/TVCG.2019.2904063
- [4] W. Bao, W.-S. Lai, C. Ma, X. Zhang, Z. Gao, and M.-H. Yang. Depth-aware video frame interpolation. In *IEEE CVPR*, 2019. doi: 10.1109/CVPR.2019.00382
- [5] S. Barannikov. Framed Morse complexes and its invariants. *Adv. Soviet Math.*, 1994. doi: 10.1090/advsov/021/03
- [6] A. C. Bauer, H. Abbasi, J. Ahrens, H. Childs, B. Geveci, S. Klasky, K. Moreland, P. O’Leary, V. Vishwanath, B. Whitlock, and E. W. Bethel. In-situ methods, infrastructures, and applications on high performance computing platforms. *CGF*, 2016. doi: 10.1111/cgf.12930
- [7] T. Bin Masood, J. Budin, M. Falk, G. Favelier, C. Garth, C. Gueunet, P. Guillou, L. Hofmann, P. Hristov, A. Kamakshidasan, C. Kappe, P. Klacansky, P. Laurin, J. Levine, J. Lukaszczuk, D. Sakurai, M. Soler, P. Steneteg, J. Tierny, W. Usher, J. Vidal, and M. Wozniak. An Overview of the Topology ToolKit. In *TopoInVis*, 2019. doi: 10.1007/978-3-030-83500-2\_16
- [8] P. Bremer, G. Weber, J. Tierny, V. Pascucci, M. Day, and J. Bell. Interactive exploration and analysis of large scale simulations using topology-based data segmentation. *IEEE TVCG*, 2011. doi: 10.1109/TVCG.2010.253
- [9] N. Brown, R. Nash, P. Poletti, G. Guzzetta, M. Manica, A. Zardini, M. Flatken, J. Vidal, C. Gueunet, E. Belikov, J. Tierny, A. Podobas, W. D. Chien, S. Markidis, and A. Gerndt. Utilising urgent computing to tackle the spread of mosquito-borne diseases. In *IEEE/ACM UrgentHPC@SC*, 2021. doi: 10.1109/UrgentHPC54802.2021.00010
- [10] M. Carrière, F. Chazal, M. Glisse, Y. Ike, H. Kannan, and Y. Umeda. Optimizing persistent homology based functions. In *ICML*, 2021. doi: 10.48550/arXiv.2010.08356
- [11] H. Chen, B. He, H. Wang, Y. Ren, S. N. Lim, and A. Shrivastava. Nerv: Neural representations for videos. *NeurIPS*, 2021. doi: 10.1109/NeurIPS.2021.3903
- [12] Z. Chen, Y. Chen, J. Liu, X. Xu, V. Goel, Z. Wang, H. Shi, and X. Wang. Videoinr: Learning video implicit neural representation for continuous space-time super-resolution. In *IEEE CVPR*, 2022. doi: 10.1109/CVPR52688.2022.00209
- [13] M. Choi, H. Kim, B. Han, N. Xu, and K. M. Lee. Channel attention is all you need for video frame interpolation. In *AAAI conference on artificial intelligence*, 2020. doi: 10.1609/aaai.v34i07.6693
- [14] D. Davis, D. Drusvyatskiy, S. M. Kakade, and J. D. Lee. Stochastic Subgradient Method Converges on Tame Functions. *FoCM*, 2020. doi: 10.1007/s10208-018-09409-5
- [15] J. Dong, K. Ota, and M. Dong. Video frame interpolation: A comprehensive survey. *ACM Trans. on MCCA*, 2023. doi: 10.1145/3556544
- [16] A. Dosovitskiy, P. Fischer, E. Ilg, P. Hausser, C. Hazirbas, V. Golkov, P. Van Der Smagt, D. Cremers, and T. Brox. FlowNet: Learning optical flow with convolutional networks. In *IEEE ICCV*, 2015. doi: 10.1109/ICCV.2015.316
- [17] H. Edelsbrunner and J. Harer. *Computational Topology: An Introduction*. 2009. doi: 10.1090/mbk/069
- [18] H. Edelsbrunner, D. Letscher, and A. Zomorodian. Topological Persistence and Simplification. *DCG*, 2002. doi: 10.1007/s00454-002-2885-2
- [19] H. Edelsbrunner and E. P. Mücke. Simulation of simplicity: a technique to cope with degenerate cases in geometric algorithms. *ACM ToG*, 1990. doi: 10.1145/77635.77639
- [20] M. Flatken, A. Podobas, R. Fellegara, A. Basermann, J. Holke, D. Knapp, M. Kontak, C. Krullikowski, M. Nolde, N. Brown, R. Nash, G. Gibb, E. Belikov, S. W. D. Chien, S. Markidis, P. Guillou, J. Tierny, J. Vidal, C. Gueunet, J. Günther, M. Pawlowski, P. Poletti, G. Guzzetta, M. Manica, A. Zardini, J.-P. Chaboureaud, M. Mendes, A. Cardil, S. Monedero, J. Ramirez, and A. Gerndt. VESTEC: Visual Exploration and Sampling Toolkit for Extreme Computing. *IEEE Access*, 2023. doi: 10.1109/ACCESS.2023.3301177
- [21] P. Frosini and C. Landi. Size theory as a topological tool for computer vision. *Pattern Recognition and Image Analysis*, 1999.
- [22] R. B. Gabrielsson, V. Ganapathi-Subramanian, P. Skraba, and L. J. Guibas. Topology-Aware Surface Reconstruction for Point Clouds. *CGF*, 2020. doi: 10.1111/cgf.14079
- [23] H. Gadirov, J. B. Roerdink, and S. Frey. Flint: Learning-based flow estimation and temporal interpolation for scientific ensemble visualization. *arXiv preprint*, 2024. doi: arXiv:2409.19178
- [24] J. Gehring, M. Auli, D. Grangier, D. Yarats, and Y. N. Dauphin. Convolutional sequence to sequence learning. In *ICML*, 2017. doi: 10.48550/arXiv.1705.03122
- [25] R. B. Girshick. Fast R-CNN. In *ICCV*, 2015. doi: 10.1109/ICCV.2015.169
- [26] P. Gu, D. Z. Chen, and C. Wang. Nervi: Compressive neural representation of visualization images for communicating volume visualization results. *Computers & Graphics*, 2023. doi: 10.1016/j.cag.2023.08.024
- [27] C. Gueunet, P. Fortin, J. Jomier, and J. Tierny. Task-Based Augmented Contour Trees with Fibonacci Heaps. *IEEE TPDS*, 2019. doi: 10.1109/TPDS.2019.2898436
- [28] C. Gueunet, P. Fortin, J. Jomier, and J. Tierny. Task-based Augmented Reeb Graphs with Dynamic ST-Trees. In *EGPGV*, 2019. doi: 10.2312/PGV.20191107
- [29] P. Guillou, J. Vidal, and J. Tierny. Discrete Morse Sandwich: Fast Computation of Persistence Diagrams for Scalar Data – An Algorithm and A Benchmark. *IEEE TVCG*, 2023. doi: 10.1109/TVCG.2023.3238008
- [30] Y. Guo, L. Bi, E. Ahn, D. Feng, Q. Wang, and J. Kim. A spatiotemporal volumetric interpolation network for 4d dynamic medical image. In *IEEE CVPR*, 2020. doi: 10.1109/CVPR42600.2020.00478
- [31] J. Han and C. Wang. Tsr-tvd: Temporal super-resolution for time-varying data analysis and visualization. *IEEE TVCG*, 2019. doi: 10.1109/TVCG.2019.2934255
- [32] J. Han and C. Wang. Coordnet: Data generation and visualization generation for time-varying volumes via a coordinate-based neural network. *IEEE TVCG*, 2022. doi: 10.1109/TVCG.2022.3197203
- [33] J. Han, H. Zheng, and C. Bi. Kd-inr: Time-varying volumetric data compression via knowledge distillation-based implicit neural representation. *IEEE TVCG*, 2023. doi: 10.1109/TVCG.2023.3345373
- [34] J. Han, H. Zheng, D. Z. Chen, and C. Wang. Stnet: An end-to-end generative framework for synthesizing spatiotemporal super-resolution volumes. *IEEE TVCG*, 2021. doi: 10.1109/TVCG.2021.3114815
- [35] K. He, X. Zhang, S. Ren, and J. Sun. Deep residual learning for image recognition. In *IEEE CVPR*, 2016. doi: 10.1109/CVPR.2016.90
- [36] C. Heine, H. Leitte, M. Hlawitschka, F. Iuricich, L. De Floriani, G. Scheuermann, H. Hagen, and C. Garth. A survey of topology-based methods in visualization. *CGF*, 2016. doi: 10.1111/cgf.12933
- [37] Z. Huang, T. Zhang, W. Heng, B. Shi, and S. Zhou. Real-time intermediate flow estimation for video frame interpolation. In *European Conference on Computer Vision*. Springer, 2022. doi: 10.1007/978-3-031-19781-9\_36
- [38] E. Ilg, N. Mayer, T. Saikia, M. Keuper, A. Dosovitskiy, and T. Brox. FlowNet 2.0: Evolution of optical flow estimation with deep networks. In *IEEE CVPR*, 2017. doi: 10.1109/CVPR.2017.179
- [39] P. Isola, J.-Y. Zhu, T. Zhou, and A. A. Efros. Image-to-image translation with conditional adversarial networks. In *IEEE CVPR*, 2017. doi: 10.1109/CVPR.2017.632
- [40] H. Jiang, D. Sun, V. Jampani, M.-H. Yang, E. Learned-Miller, and J. Kautz. Super slo-mo: High quality estimation of multiple intermediate frames for video interpolation. In *IEEE CVPR*, 2018. doi: 10.1109/CVPR.2018.00938
- [41] C. Jiao, C. Bi, and L. Yang. Ffeinr: flow feature-enhanced implicit neural representation for spatiotemporal super-resolution. *Journal of Visualization*, 2024. doi: 10.1007/s12650-024-00959-1
- [42] T. Kalluri, D. Pathak, M. Chandraker, and D. Tran. Flavr: Flow-agnostic video representations for fast frame interpolation. In *WACV*,

2023. doi: 10.1109/WACV56688.2023.00211
- [43] D. P. Kingma and J. Ba. Adam: A method for stochastic optimization. In *ICLR*, 2015. doi: 10.48550/arXiv.1412.6980
- [44] M. Kissi, M. Pont, J. A. Levine, and J. Tierny. A Practical Solver for Scalar Data Topological Simplification. *IEEE TVCG*, 2024. doi: 10.1109/TVCG.2024.3456345
- [45] T. Lacombe, M. Cuturi, and S. Oudot. Large Scale computation of Means and Clusters for Persistence Diagrams using Optimal Transport. In *NIPS*, 2018. doi: 10.48550/arXiv.1805.08331
- [46] H. Lee, T. Kim, T.-y. Chung, D. Pak, Y. Ban, and S. Lee. Adacof: Adaptive collaboration of flows for video frame interpolation. In *IEEE CVPR*, 2020. doi: 10.1109/CVPR42600.2020.00536
- [47] Y. Li, X. Liang, B. Wang, Y. Qiu, L. Yan, and H. Guo. Msz: An efficient parallel algorithm for correcting morse-smale segmentations in error-bounded lossy compressors. *IEEE TVCG*, 2025. doi: 10.1109/TVCG.2024.3456337
- [48] P. Lindstrom. Fixed-Rate Compressed Floating-Point Arrays. *IEEE TVCG*, 2014. doi: 10.1109/TVCG.2014.2346458
- [49] Y. Liu, L. Xie, L. Siyao, W. Sun, Y. Qiao, and C. Dong. Enhanced quadratic video interpolation. In *ECCV Workshops*. Springer, 2020. doi: 10.1007/978-3-030-66823-5\_3
- [50] Y. Lu, P. Gu, and C. Wang. Fcnrr: Fast compressive neural representation of visualization images. In *VIS. IEEE*, 2024. doi: 10.1109/VIS55277.2024.00014
- [51] Y. Lu, K. Jiang, J. A. Levine, and M. Berger. Compressive neural representations of volumetric scalar fields. In *CGF*, 2021. doi: 10.1111/cgf.14295
- [52] B. D. Lucas and T. Kanade. An iterative image registration technique with an application to stereo vision. In *IJCAI*, pp. 674–679, 1981.
- [53] J. Lukaszczuk, M. Will, F. Wetzels, G. H. Weber, and C. Garth. Ex-TreeM: Scalable Augmented Merge Tree Computation via Extremum Graphs. *IEEE TVCG*, 2024. doi: 10.1109/TVCG.2023.3326526
- [54] S. Meyer, O. Wang, H. Zimmer, M. Grosse, and A. Sorkine-Hornung. Phase-based frame interpolation for video. In *IEEE CVPR*, 2015. doi: 10.1109/CVPR.2015.7298747
- [55] F. Nauleau, F. Vivodtzev, T. Bridel-Bertomeu, H. Beaugendre, and J. Tierny. Topological Analysis of Ensembles of Hydrodynamic Turbulent Flows – An Experimental Study. In *IEEE LNAV*, 2022. doi: 10.1109/LNAV57265.2022.9966403
- [56] A. Nigmatov and D. Morozov. Topological optimization with big steps. *DCG*, 2022. doi: 10.1007/s00454-023-00613-x
- [57] S. Niklaus and F. Liu. Softmax splatting for video frame interpolation. In *IEEE CVPR*, 2020. doi: 10.1109/CVPR42600.2020.00548
- [58] S. Niklaus, L. Mai, and F. Liu. Video frame interpolation via adaptive separable convolution. In *IEEE ICCV*, 2017. doi: 10.1109/ICCV.2017.37
- [59] M. Olejniczak and J. Tierny. Topological Data Analysis of Vortices in the Magnetically-Induced Current Density in LiH Molecule. *PCCP*, 2023. doi: 10.1039/D2CP05893F
- [60] J. Park, K. Ko, C. Lee, and C.-S. Kim. Bmbc: Bilateral motion estimation with bilateral cost volume for video interpolation. In *ECCV*. Springer, 2020. doi: 10.1007/978-3-030-58568-6\_7
- [61] J. Park, C. Lee, and C.-S. Kim. Asymmetric bilateral motion estimation for video frame interpolation. In *IEEE ICCV*, 2021. doi: 10.1109/ICCV48922.2021.01427
- [62] A. Paszke, S. Gross, F. Massa, A. Lerer, J. Bradbury, G. Chanan, T. Killeen, Z. Lin, N. Gimelshein, L. Antiga, A. Desmaison, A. Köpf, E. Z. Yang, Z. DeVito, M. Raison, A. Tejani, S. Chilamkurthy, B. Steiner, L. Fang, J. Bai, and S. Chintala. PyTorch: An Imperative Style, High-Performance Deep Learning Library. In *NeurIPS*, 2019. doi: 10.48550/arXiv.1912.01703
- [63] J. Patchett and G. R. Gislér. The IEEE SciVis Contest. <https://oceans11.lanl.gov/deepwaterimpact/>, 2018.
- [64] M. Pont and J. Tierny. Wasserstein Auto-Encoders of Merge Trees (and Persistence Diagrams). *IEEE TVCG*, 2024. doi: 10.1109/TVCG.2023.3334755
- [65] M. Pont, J. Vidal, J. Delon, and J. Tierny. Wasserstein Distances, Geodesics and Barycenters of Merge Trees. *IEEE TVCG*, 2022. <https://github.com/MatPont/WassersteinMergeTreesData>. doi: 10.1109/TVCG.2021.3114839
- [66] M. Pont, J. Vidal, and J. Tierny. Principal Geodesic Analysis of Merge Trees (and Persistence Diagrams). *IEEE TVCG*, 2023. doi: 10.1109/TVCG.2022.3215001
- [67] A. Poulenard, P. Skraba, and M. Ovsjanikov. Topological function optimization for continuous shape matching. *CGF*, 2018. doi: 10.1111/cgf.13487
- [68] F. Reda, J. Kontkanen, E. Tabellion, D. Sun, C. Pantofaru, and B. Curless. Film: Frame interpolation for large motion. In *ECCV*, 2022. doi: 10.1007/978-3-031-20071-7\_15
- [69] V. Robins. Toward computing homology from finite approximations. *Topology Proceedings*, 1999.
- [70] V. Robins, P. J. Wood, and A. P. Sheppard. Theory and Algorithms for Constructing Discrete Morse Complexes from Grayscale Digital Images. *IEEE Trans. PAMI*, 2011. doi: 10.1109/TPAMI.2011.95
- [71] N. Shivashankar, P. Pranav, V. Natarajan, R. van de Weygaert, E. P. Bos, and S. Rieder. Felix: A topology based framework for visual exploration of cosmic filaments. *IEEE TVCG*, 2016. doi: 10.1109/TVCG.2015.2452919
- [72] M. Soler, M. Petitfrère, G. Darche, M. Plainchault, B. Conche, and J. Tierny. Ranking Viscous Finger Simulations to an Acquired Ground Truth with Topology-Aware Matchings. In *IEEE LNAV*, 2019. doi: 10.48550/arXiv.1908.07841
- [73] M. Soler, M. Plainchault, B. Conche, and J. Tierny. Topologically controlled lossy compression. In *PacificViz*, 2018. doi: 10.48550/arXiv.1802.02731
- [74] E. Solomon, A. Wagner, and P. Bendich. A fast and robust method for global topological functional optimization. In *AISTATS*, 2021. doi: 10.48550/arXiv.2009.08496
- [75] D. Sun, X. Yang, M.-Y. Liu, and J. Kautz. Pwc-net: Cnns for optical flow using pyramid, warping, and cost volume. In *IEEE CVPR*, 2018. doi: 10.1109/CVPR.2018.00931
- [76] K. Tang and C. Wang. Stsr-inr: Spatiotemporal super-resolution for multivariate time-varying volumetric data via implicit neural representation. *Computers & Graphics*, 2024. doi: 10.1016/j.cag.2024.01.001
- [77] Z. Teed and J. Deng. Raft: Recurrent all-pairs field transforms for optical flow. In *ECCV*. Springer, 2020. doi: 10.1007/978-3-030-58536-5\_24
- [78] J. Tierny, G. Favelier, J. A. Levine, C. Gueunet, and M. Michaux. The Topology Toolkit. *IEEE TVCG*, 2017. doi: 10.1109/TVCG.2017.2743938
- [79] TTK Contributors. TTK Data. <https://github.com/topology-tool-kit/ttk-data/>, 2020.
- [80] K. Turner, Y. Mileyko, S. Mukherjee, and J. Harer. Fréchet Means for Distributions of Persistence Diagrams. *DCG*, 2014. doi: 10.1007/s00454-014-9604-7
- [81] D. Ulyanov, A. Vedaldi, and V. Lempitsky. Instance normalization: The missing ingredient for fast stylization. *arXiv preprint*, 2016. doi: 10.48550/arXiv.1607.08022
- [82] A. Vaswani, N. Shazeer, N. Parmar, J. Uszkoreit, L. Jones, A. N. Gomez, L. Kaiser, and I. Polosukhin. Attention is all you need. In *NeurIPS*, 2017. doi: 10.48550/arXiv.1706.03762
- [83] L. Wan, M. Zeiler, S. Zhang, Y. LeCun, and R. Fergus. Regularization of neural networks using dropconnect. In *ICML*, 2013. doi: 10.5555/3042817.3043055
- [84] W. Wang, C. Bruyere, B. Kuo, and T. Scheitlin. The IEEE SciVis Contest. <http://sciviscontest.ieeevis.org/2004/>, 2004.
- [85] Z. Wang, J. Liu, X. Chen, G. Li, and H. Han. Sparse self-attention aggregation networks for neural sequence slice interpolation. *BioData Mining*, 2021. doi: 10.1186/s13040-021-00236-z
- [86] Q. Wu, D. Bauer, Y. Chen, and K.-L. Ma. Hyperinr: A fast and predictive hypernetwork for implicit neural representations via knowledge distillation. *arXiv preprint*, 2023. doi: arXiv:2304.04188
- [87] L. Yan, Y. Wang, E. Munch, E. Gasparovic, and B. Wang. A structural average of labeled merge trees for uncertainty visualization. *IEEE TVCG*, 2019. doi: 10.1109/TVCG.2019.2934242
- [88] X.-I. Yin, D.-x. Liang, L. Wang, J. Qiu, Z.-y. Yang, J.-z. Dong, and Z.-y. Ma. Analysis of coronary angiography video interpolation methods to reduce x-ray exposure frequency based on deep learning. *Cardio-vascular Innov. and App.*, 2021. doi: 10.15212/CVIA.2021.0011